ACS NANO

www.acsnano.org

ARTICLE

Vertically Aligned Mesoporous Arrays Catalyzing Long-Chain Polysulfide Conversion to Unlock High-Energy Magnesium–Sulfur Batteries

Xian Zhou, Tian Xu, Miao Guo, Hongyu Zhang, Chaoqun Li, Wenbin Wang, Ming Sun, Guanglin Xia, and Xuebin Yu*

Cite This: *ACS Nano* 2025, 19, 31224–31235

Read Online

ACCESS | Metrics & More | Article Recommendations | Supporting Information

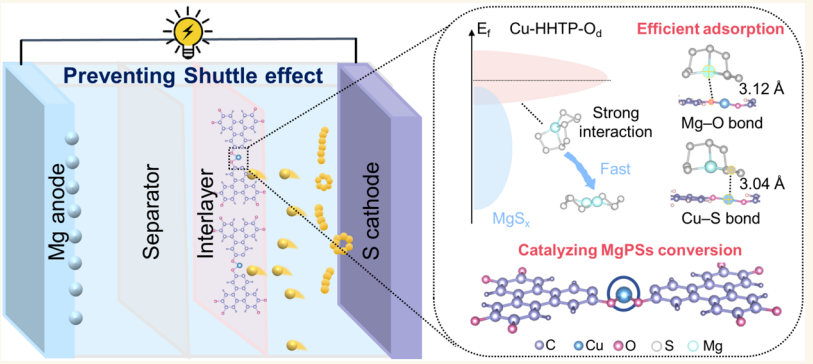

ABSTRACT: **Rechargeable magnesium–sulfur (Mg–S) batteries are attractive for next-generation energy storage systems owing to their safety and superior volumetric energy density. Nevertheless, the underlying origins of the severe shuttle effect in Mg–S batteries remain unclear, significantly limiting improvements in their electrochemical performance. Herein, insufficient MgS_8 conversion kinetics is identified as the primary cause of the shuttle effect in Mg–S batteries. A thermally activated metal–organic framework (MOF)-derived cuprous 2,3,6,7,10,11-triphenylenehexol (Cu-HHTP-200@CNT) interlayer with vertically aligned mesoporous arrays is designed to modulate sulfur conversion kinetics. The reduced spatial hindrance within the mesopores facilitates the preconcentration of long-chain polysulfides, while coordinatively unsaturated Cu sites establish catalytic interfaces through sufficient *d–p* orbital hybridization. Consequently, the optimized S-Cu-HHTP-200@CNT configuration elevates the main discharge plateau from 1.1 to 1.6 V, achieves a high-rate performance (a power density of 4090 W kg^{-1} after 500 cycles at 3 C), and maintains a capacity of 236 mAh g^{-1} at −20 °C. This work highlights the critical role of electrocatalytic regulation in long-chain sulfur conversion and provides design principles for high-performance sulfur-based batteries.**

KEYWORDS: *conductive metal–organic framework, mesoporous materials, functional interlayer, sulfur redox catalysis, Mg–S batteries*

1. INTRODUCTION

The escalating demand for high safety, volumetric capacity, and extended cycle life in energy storage devices is propelling the development of multivalent ion batteries. In the past decade, rechargeable magnesium–sulfur (Mg–S) batteries are a promising system owing to a theoretical specific energy density of 1722 Wh kg^{-1} and the use of earth-abundant Mg and S as the anode and cathode, respectively.[1−3] However,

Received: June 20, 2025
Revised: August 14, 2025
Accepted: August 14, 2025
Published: August 21, 2025

https://doi.org/10.1021/acsnano.5c10366
ACS Nano 2025, 19, 31224–31235

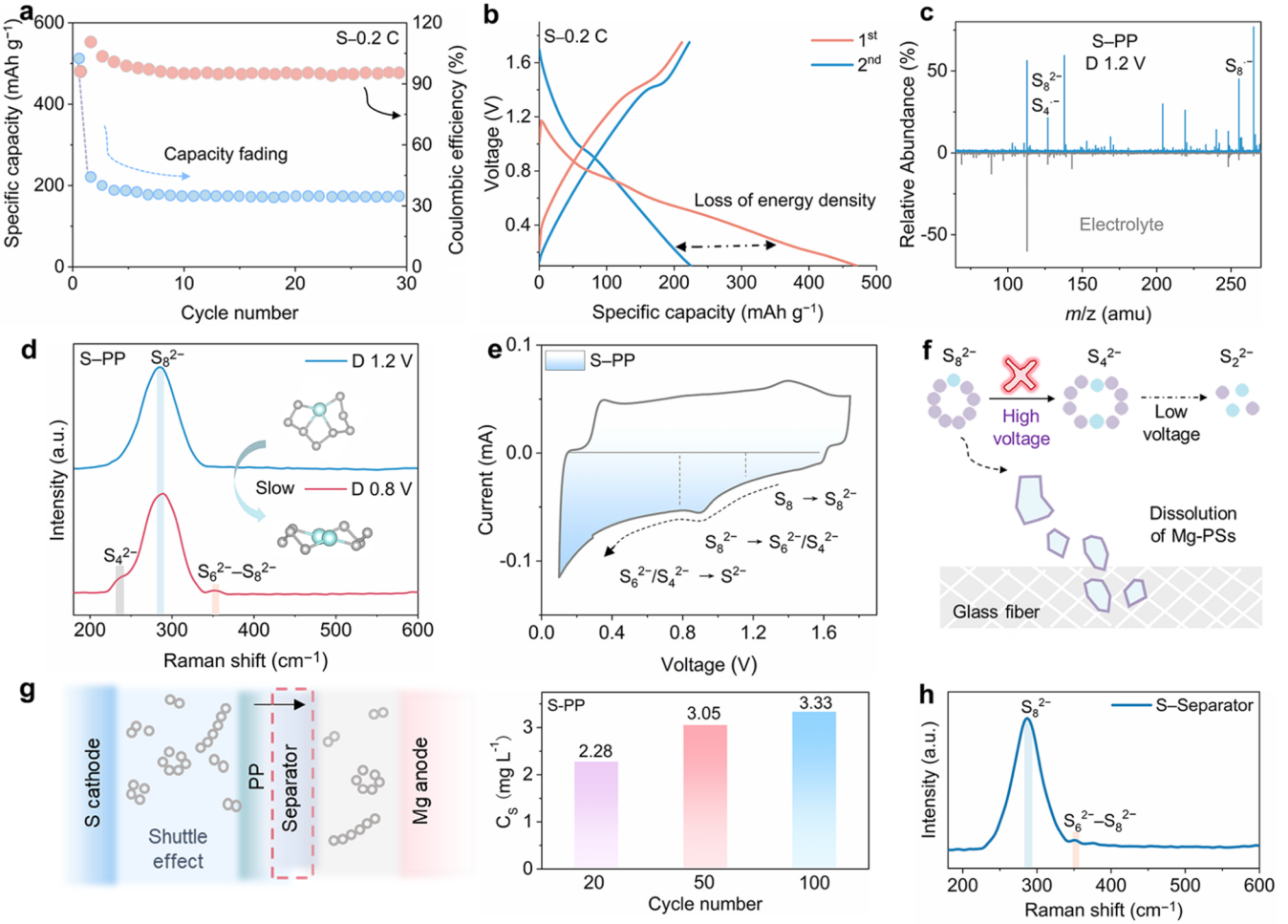

Figure 1. (a) Cycling performance, (b) galvanostatic charge−discharge curves of the S cathode in APC hybrid electrolyte at 0.2 C. (c) MS of the PP interlayer from S−PP batteries after discharge to 1.2 V. (d) Raman spectra of the PP interlayer at different discharge states in Mg−S batteries (gray and cyan spheres representing S and Mg atoms, respectively). (e) *C*−*V* curve of S−PP. (f) Schematic illustration of the stepwise reduction of polysulfide anions and the capacity degradation mechanism. (g) The content of sulfur element on the separator after different cycles from ICP analysis. (h) Raman spectra of the separator after 100 cycles in Mg−S batteries.

there are several unsolved problems that hinder the practical application of Mg−S batteries, including unsatisfactory rate capabilities, cycling stability, and low-temperature (LT) operation. These limitations largely stem from the complex sulfur reduction mechanism, where S_8 converts to MgS via magnesium polysulfide intermediates (MgS_x, $4 \leq x \leq 8$), with soluble long-chain species shuttling between electrodes.[4,5] Hence, identifying specific polysulfide species that are responsible for shuttle behavior and battery failure is crucial for the targeted regulation of electrochemical performance in Mg−S batteries.

Generally, long-chain polysulfides exhibit a competitive interplay between the dissolution and conversion processes. Dominant dissolution exacerbates the shuttling effect, which could result in active materials loss, anode corrosion, and capacity degradation, while conversion-dominated pathways could promote the formation of the multiple MgS_x species. According to Le Chatelier's principle, the elevated polysulfide concentration accelerates conversion rates in each consecutive step, thereby favoring higher capacity.[6,7] This means that regulating conversion and reducing accumulation of MgS_x are critical to improving redox kinetics and long-term stability.[7] Unfortunately, the relationship between long-chain MgS_x and the kinetic performance has not yet been established.

Polar catalysts (*e.g.*, Cu_3P, Zn single atoms) have shown effectiveness in achieving high discharge capacity through the chemical adsorption of polysulfides.[8,9] Additionally, incorporating composite electrocatalysts (*e.g.*, ZIF-67 derivative carbon host, MXene-TiO_2@rGO) could immobilize polysulfides and facilitate conversion kinetics.[10−12] However, the catalytic effect of these materials is often compromised by inhomogeneous distribution and poor interfacial contact between catalytic sites and S-containing species.[13] These kinetic limitations prevent Mg−S batteries from operating at rates above 2 C (1 C = 1675 mA g^{-1}) or under subzero temperatures. A rationally designed interlayer positioned between the cathode and separator could increase their contact, which incorporates conductive matrices, optimal adsorbents, and catalysts.[13,14] In this regard, the ordered porous structures and abundant active sites make conductive conjugated coordination polymers (CCPs) promising in Mg−S batteries.[15−19] Nevertheless, the saturated coordination environment of metal nodes in electrocatalyst restrains efficient adsorption and catalytic activity.[20] Therefore, it is essential to precisely modulate the coordination environment of metal sites and understand the

https://doi.org/10.1021/acsnano.5c10366
ACS Nano 2025, 19, 31224−31235

complex interactions between metal sites and MgS_x species, particularly their impacts on capacity retention and reversibility. Unveiling these fundamental mechanisms is an important prerequisite for achieving high-performance Mg−S batteries.

Employing this insight, we present a comprehensive investigation that identifies the sluggish conversion of MgS_8 as the primary cause of capacity degradation in Mg−S batteries. The thermally activated cuprous 2,3,6,7,10,11-triphenylenehexol (Cu-HHTP-200) with vertically aligned mesoporous arrays is employed to shorten ion transport pathways and provides a confined microenvironment for the enrichment of long-chain polysulfides. The abundant coordinatively unsaturated Cu sites within the mesoporous channels enhance robust electronic interaction between Cu *d*-bands and S *p*-states, strengthen the binding affinity toward MgS_x species, and reduce the conversion barrier of MgS_8. Beneficial from the above merits, the liquid-phase conversion from MgS_8 to MgS_4 is accomplished at an elevated platform (from 1.1 to 1.6 V), favorable for kinetic properties. Consequently, the Mg−S batteries incorporating Cu-HHTP-based interlayers deliver an enlarged discharge capacity and enhanced rate performance even at −20 °C. This work unveils the pivotal function of mesoporous materials in facilitating efficient preconcentration of long-chain polysulfides, while also elucidating the positive impact of the rapid conversion of liquid-phase long-chain polysulfides on the kinetic performance.

2. RESULTS AND DISCUSSION

2.1. Capacity Degradation Mechanisms of the S Cathode. The electrochemical cycling performance of the S cathode was first evaluated in a conventional 0.4 mol L^{-1} $(PhMgCl)_2$−$AlCl_3$ (APC) hybrid electrolyte. The S cathode demonstrates rapid capacity deterioration, declining from 471 to 220 mAh g^{-1} within 10 cycles, as illustrated in Figure 1a. Notably, the galvanostatic profiles (Figure 1b) reveal the specific energy decreased from 241 to 154 Wh kg^{-1} in the second cycle. After excluding electrolyte decomposition via linear sweep voltammetry (Figure S1a), we employed mass spectrometry (MS) to probe the fundamental origin of the performance decay by tracking the evolution of discharge products (Figure 1c). Upon discharge to 1.2 V, substantial accumulation of long-chain polysulfide anions ($S_8^{\bullet-}$) was detected on the polypropylene (PP) interlayer, but S_8^{2-} and $S_4^{\bullet-}$ species remain indistinguishable due to their identical mass-to-charge ratios (m/z). Raman spectroscopy was further investigated to identify the various types of polysulfide anions (Figure 1d). As the discharge progresses to 1.2 V, the dominant peak at 285 cm^{-1} confirms the accumulation of S_8^{2-}, free from experimental artifacts (Figure S1b).[21] Upon discharge to 0.8 V, although weak signals of S_6^{2-} and S_4^{2-} (245 and 357 cm^{-1}, respectively) emerged, the predominant peaks corresponding to S_8^{2-} reveal severely limited reduction of MgS_8.[22,23]

To comprehensively understand the stepwise reduction mechanism, cyclic voltammetry (C−V) analysis was performed (Figure 1e). Based on the above spectroscopic characterizations, the electrochemical reduction of S−PP can be delineated into three distinct stages. Initially, S_8 converts to S_8^{2-} between 1.6 and 1.2 V, followed by partial reduction of S_8^{2-} to S_6^{2-}/S_4^{2-} between 1.2 and 0.8 V, and finally transformation to S_2^{2-}/S^{2-}.[24] The sluggish kinetics in the second stage results in substantial accumulation of soluble S_8^{2-} species, which subsequently diffuse through the separator driven by concentration gradients (Figure 1f). This shuttling behavior was quantitatively verified by tracking the sulfur content in the separator using inductively coupled plasma (ICP) spectroscopy (Figure 1g). The progressive increase in sulfur concentration during cycling, coupled with the predominant S_8^{2-} signals in Raman analysis (Figure 1h), provides direct evidence that the limited kinetics of MgS_8-to-MgS_4 conversion constitutes the fundamental cause of the shuttle effect.

The continuous shuttling of polysulfides induces irreversible structural evolution of both electrodes, as revealed by post-mortem analysis after 10 cycles at 0.2 C. Scanning electron microscopy (SEM), transmission electron microscopy (TEM), and related analyses (Figures S2−S8) confirm that sulfur is uniformly distributed across the hollow nanospheres synthesized via a polystyrene-template-assisted method. However, after cycling, significant bulk agglomeration occurs, with particle sizes ranging from 1 to 10 μm (Figure S9). Moreover, cross-sectional analyses demonstrate a nearly 2-fold expansion in the volume of the S cathode during cycling, which may be attributed to the formation of low-density MgS.[25] On the anode side, the uneven deposition of Mg may compromise interfacial stability and electrochemical reversibility (Figure S10).[26] The aforementioned observations demonstrate that the MgS_x shuttle effect induces irreversible morphological transformations on both the S cathode and Mg anode within merely 10 cycles.

Therefore, our findings highlight three critical challenges in conventional Mg−S batteries: (i) the sluggish conversion kinetics from S_8^{2-} to S_4^{2-} results in accumulation of soluble intermediates; (ii) then, these long-chain polysulfides readily migrate toward the Mg anode in ether-based electrolytes, driven by concentration gradients;[27] (iii) thus, the accumulation and subsequent migration of polysulfides trigger irreversible structural evolution at electrode surfaces, which severely deteriorates the long-term cycling stability of Mg−S batteries.[7] While previous studies have mainly addressed polysulfide shuttling through confinement and adsorption approaches, our mechanistic investigation reveals that facilitating the conversion of MgS_8 may offer a fundamental perspective for improving sulfur redox reversibility.

2.2. Design of Cu-HHTP-Based Catalytic Interlayers. The aforementioned analyses reveal that the sluggish conversion kinetics of MgS_8 and subsequent shuttling are the primary causes of capacity decay in Mg−S batteries. To address these challenges simultaneously, we propose the incorporation of a functional interlayer that could serve as both a secondary polysulfide barrier to confine soluble MgS_x species and an electrocatalyst to accelerate sulfur redox kinetics. Among various materials, CCPs have emerged as promising candidates due to their porous structure and tunable chemical properties.[15,28] Based on these considerations, two-dimensional Cu-HHTP was selected as an adsorbent for polysulfides. SEM, Brunauer−Emmett−Teller (BET) surface area analysis, and X-ray photoelectron spectroscopy (XPS) analyses confirm the successful synthesis of Cu-HHTP (Figures S11−S13). In the extended X-ray absorption fine structure (EXAFS) spectrum, a characteristic Cu−O peak at 1.50 Å was detected. The average Cu−O coordination number of 3.3 approaches saturation, which potentially limits the exposure of Cu nodes and consequently constrains the

https://doi.org/10.1021/acsnano.5c10366
ACS Nano 2025, 19, 31224−31235

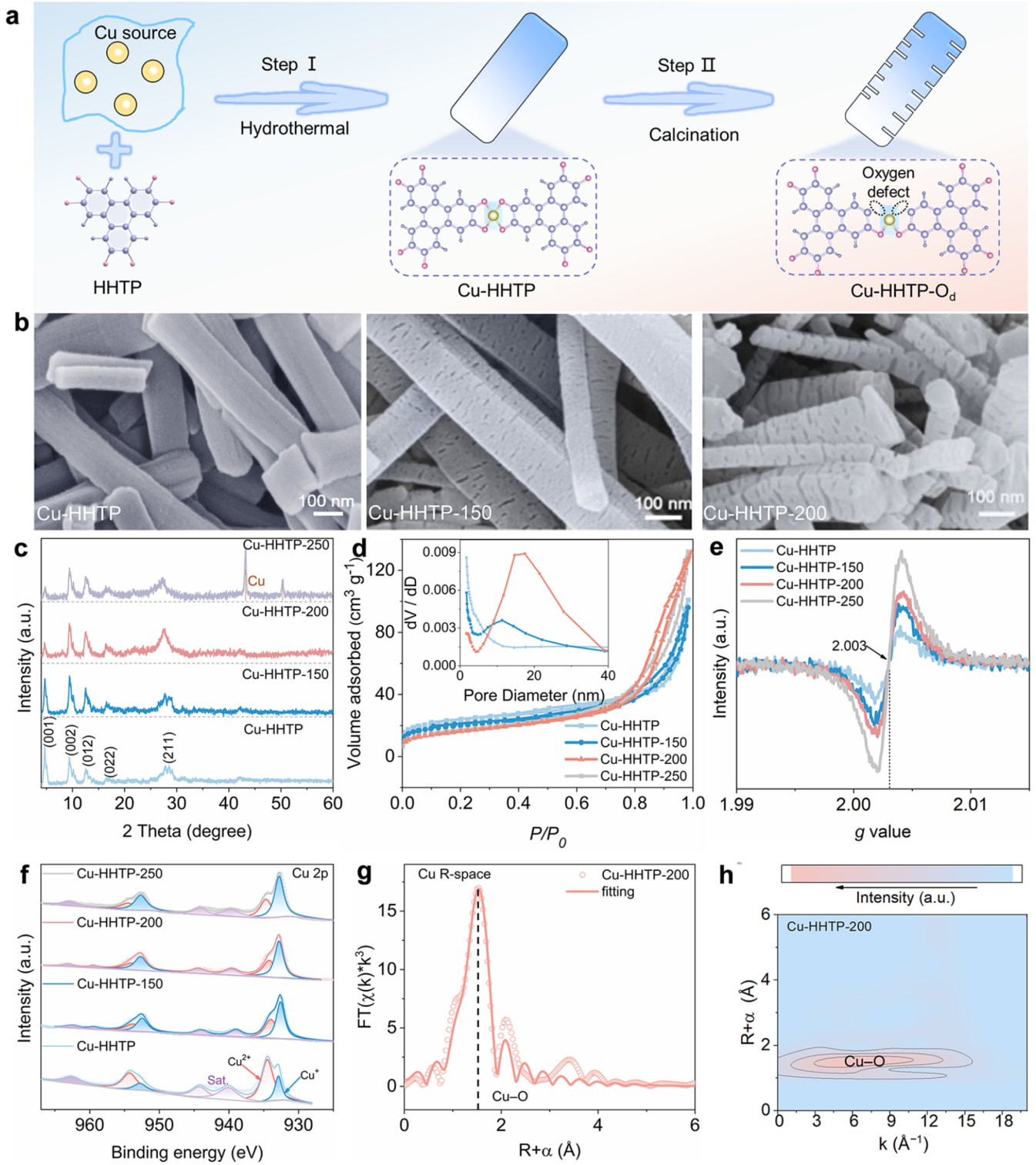

Figure 2. (a) Schematic representation of the synthesis process for Cu-HHTP and Cu-HHTP-O_d (purple, pink, and yellow spheres representing C, O, and Cu atoms, respectively). (b) SEM images of Cu-HHTP, Cu-HHTP-150 and Cu-HHTP-200. (c) XRD patterns, (d) N_2 adsorption−desorption isotherms (inset shows pore size distribution), (e) EPR spectra, and (f) XPS spectra of Cu 2p for Cu-HHTP, Cu-HHTP-150, Cu-HHTP-200, and Cu-HHTP-250. (g) Fitting analysis in R space, (h) wavelet transform analysis of Cu-HHTP-200.

enhancement of catalytic activity (Figure S13c−h and Table S1). Given that the strong anchoring of various polysulfides requires abundant *d*−*p* orbital hybridization, exposing metal sites to create unsaturated catalytic interfaces is essential.[29]

Calcination serves as an effective approach to partially remove organic ligands and generate oxygen defects adjacent to Cu sites.[30] Cu-HHTP was treated at temperatures below 200 °C (denoted as Cu-HHTP-O_d), as shown in Figure 2a. The temperature-dependent structural evolution was investigated by calcining the samples at different temperatures (150,

https://doi.org/10.1021/acsnano.5c10366
ACS Nano 2025, 19, 31224−31235

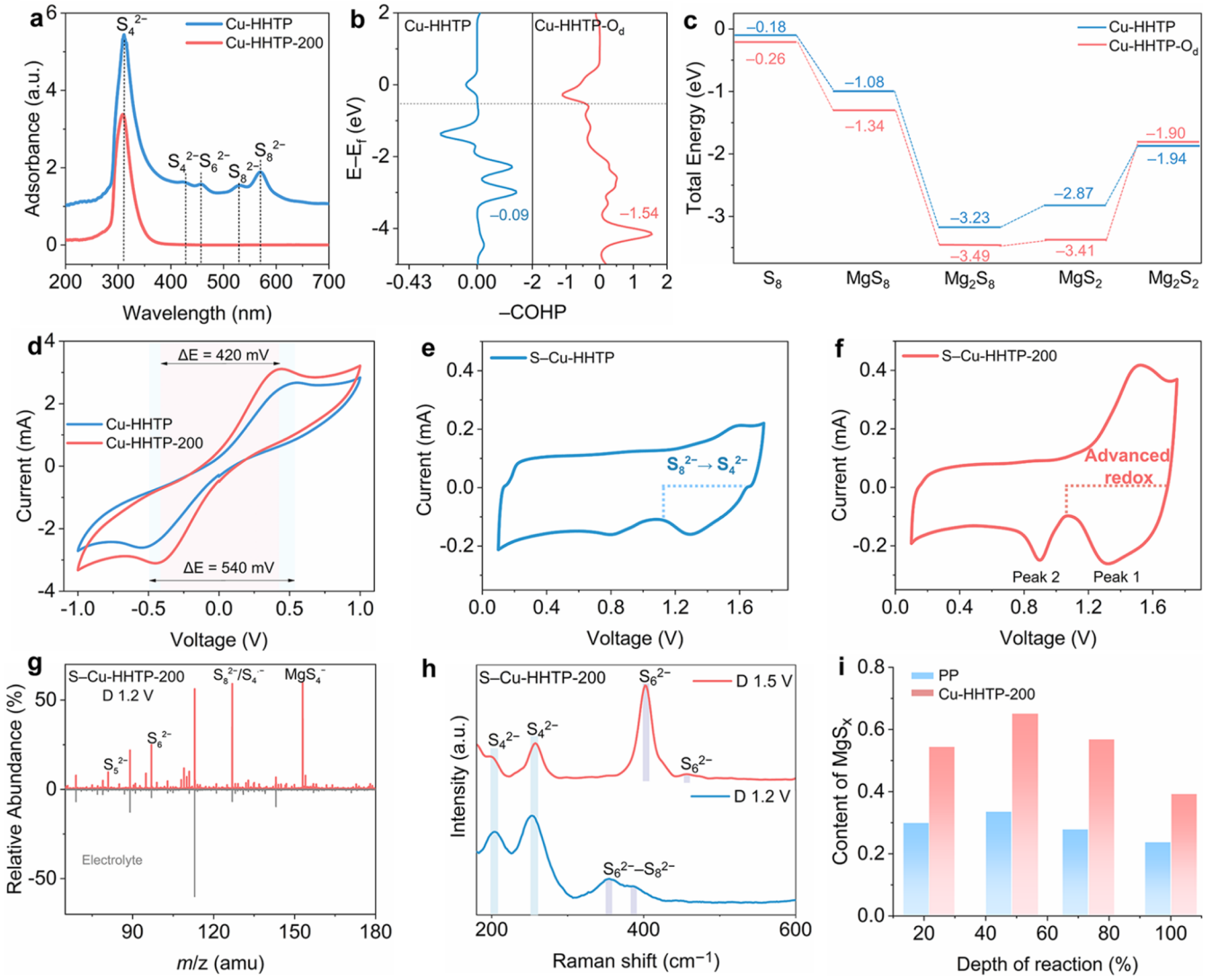

Figure 3. (a) UV–vis absorption spectra of MgS_x solution after adsorption tests with Cu-HHTP and Cu-HHTP-200 powders. (b) iCOHP analysis of MgS_8 adsorbed on Cu-HHTP and Cu-HHTP-O_d. (c) Total energy profiles of MgS_x absorbed on Cu-HHTP and Cu-HHTP-O_d. (d) *C–V* curves of symmetrical cells with different MOFs in the MgS_x solution. (e, f) *C–V* curves of Mg–S batteries with various interlayers at a scan rate of 1 mV s^{-1}. (g) MS of the Cu-HHTP-200 interlayer from S-Cu-HHTP-200 after discharge to 1.2 V. (h) Raman spectra of the Cu-HHTP-200 interlayer at different discharge states of S-Cu-HHTP-200. (i) Variation in sulfur species on the surface of the PP and Cu-HHTP-200 interlayer from XPS analysis.

200, and 250 °C) to obtain Cu-HHTP-150, Cu-HHTP-200, and Cu-HHTP-250, respectively. SEM images reveal that, as the calcination temperature increases, vertically aligned porous structures gradually develop on the surface of hexagonal rod-like crystals (Figure 2b). At 250 °C, the prismatic structures show considerable thinning, accompanied by the formation of penetrating longitudinal cracks (Figure S14). Upon further temperature elevation to 300 °C, the prismatic structures completely decompose into agglomerated blocks. The preservation of the crystalline structure of the calcined Cu-HHTP was confirmed by XRD analysis (Figure 2c). In contrast, thermal treatment above 250 °C led to the collapse of the coordination framework and the formation of metallic Cu (Figure S15). The presence of metallic Cu shifts the electrochemical reduction process from sulfur species to copper sulfides, which leads to a deviation from the characteristic redox chemistry of Mg–S batteries.[31] Moreover, the effect of calcination on pore structure is illustrated in Figure 2d and Table S2. For Cu-HHTP-200, mesopores centered around 19 nm are formed within the intrinsic microporous framework. This hierarchical porous structure consistent with SEM observations is expected to enhance both adsorption capacity and catalytic activity.[32] To further probe the structural evolution during thermal treatment, infrared spectroscopy was used (Figure S16a). The broadening of the infrared peaks at 250 °C indicates partial decoupling of the organic ligand framework. Therefore, Cu-HHTP-200 is the most suitable material for achieving a highly porous structure while maintaining the integrity of the framework.

Further investigations were conducted to examine the effect of calcination on the chemical states. Electron paramagnetic resonance (EPR) analysis in Figure 2e indicates that as the temperature rises, the number of oxygen defects increases, potentially contributing to enhanced catalytic activity.[30] As shown in Figure 2f and Figure S16b–d, the XPS spectra of Cu-HHTP and thermally treated Cu-HHTP samples (150–

https://doi.org/10.1021/acsnano.5c10366
ACS Nano 2025, 19, 31224–31235

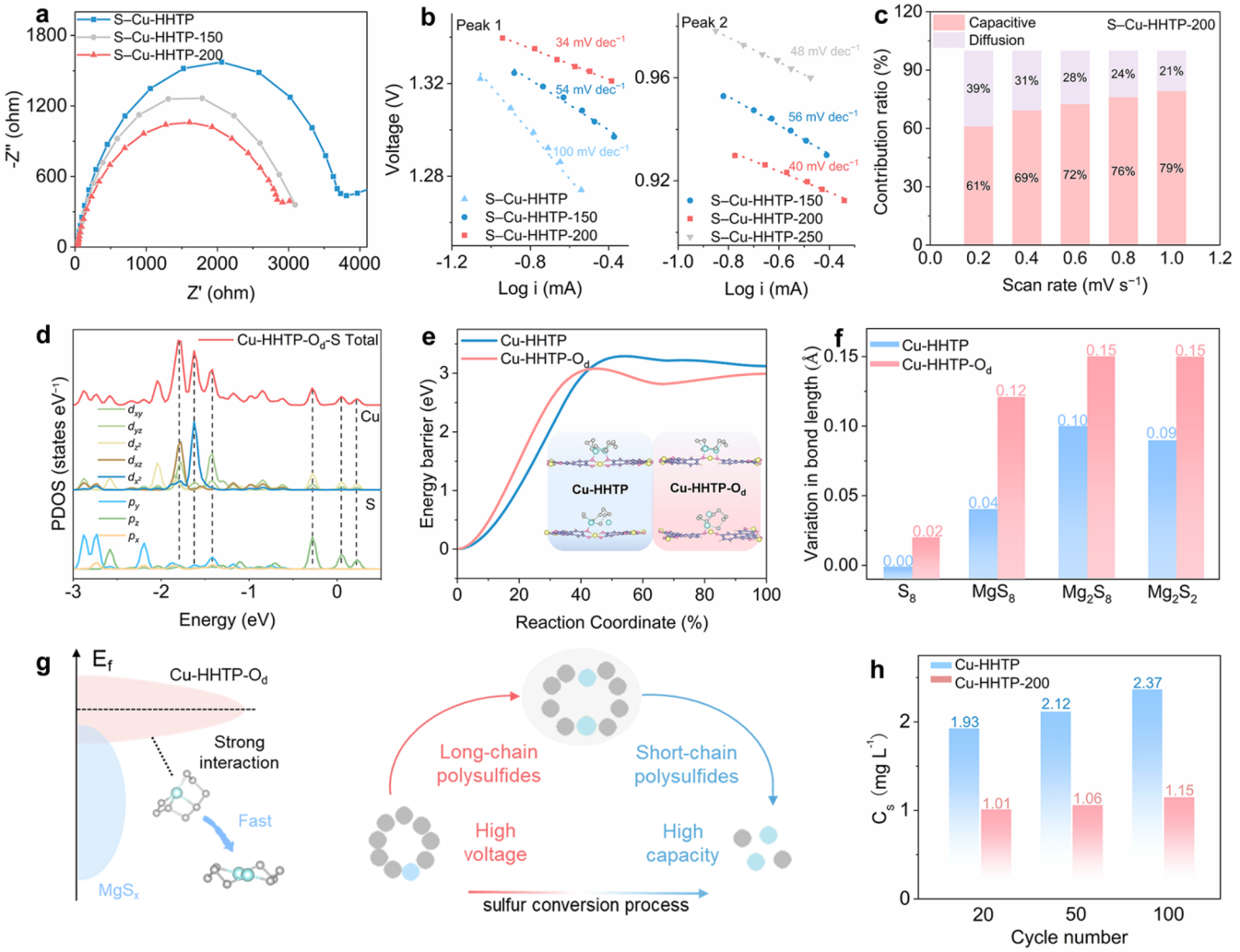

Figure 4. (a) EIS spectra of S-Cu-HHTP, S-Cu-HHTP-150, and S-Cu-HHTP-200 in the APC hybrid electrolyte. (b) Tafel plots for peak 1 and peak 2, derived from *C*−*V* curves. (c) Capacitive contribution ratios at 0.2−1 mV s^{-1}. (d) Calculated PDOS of MgS_8 adsorbed on Cu-HHTP-O_d. (e) Decomposition barriers of Mg_2S_8 (inset: adsorption configurations after decomposition). (f) Variation in Mg−S bond lengths on Cu-HHTP and Cu-HHTP-O_d substrates. (g) Schematic illustration depicting the strong catalytic interactions between MgS_x and Cu-HHTP-O_d and the sulfur reduction pathway (gray and cyan spheres representing S and Mg atoms, respectively). (h) The content of sulfur species on the separator after different cycles from the ICP analysis.

250 °C) were carefully fitted. The characteristic peaks located at 932.9 and 952.8 eV were assigned to Cu^+ $2p_{3/2}$ and $2p_{1/2}$, respectively, while the peaks at 934.5 and 954.3 eV, accompanied by satellite features, correspond to Cu^{2+}.[33,34] With increasing calcination temperature, the Cu^+ species gradually become predominant, while the Cu^{2+} signal and its satellite structure are progressively suppressed. This evolution provides credible indirect evidence for the formation of oxygen defects in coordination-based materials.[35] This attests to the fact that through calcination, a greater number of Cu^+ species can be stabilized through Cu−O coordination, which may have a positive effect on catalysis.[32] Consequently, Cu-HHTP-200 with abundant oxygen defects was selected to examine the impact of calcination on the coordination structure.

X-ray absorption near-edge spectroscopy (XANES) and EXAFS provide detailed insights into the evolution of the Cu coordination environment during thermal treatment. The white-line peak position of Cu-HHTP and Cu-HHTP-200 in Cu K-edge spectra (Figure S16e) was observed between Cu_2O and CuO references, with the oxidation state determined to lie between +1 and +2, consistent with XPS results. The Cu−O coordination architecture in Cu-HHTP-200 was found to be preserved through EXAFS fitting (Figures 2g and S16f) and wavelet transform analysis (Figure 2h). A reduction in Cu−O coordination number from 3.3 to 2.5 (Table S1) signifies the generation of abundant unsaturated Cu sites.[10] All these findings collectively indicate the successful fabrication of Cu-HHTP-200, which features an abundant hierarchical micro-mesoporous architecture, numerous oxygen defects, and highly exposed Cu sites. These structural characteristics are expected to play a vital role in facilitating sulfur redox reactions.

2.3. Catalytic Conversion Mechanism of MgS_x. The polysulfide adsorption ability of the catalytic materials was first examined to reveal the confinement role of the mesoporous structure. Both MOFs powders were immersed in MgS_x solution for adsorption experiments (Figure 3a). Due to the disproportionation reaction of S^{2-}, peaks from S_4^{2-} to S_8^{2-} were observed in UV tests, indicating the coexistence of multiple soluble MgS_x in tetrahydrofuran. Attributed to the inherent pores in the coordination structure, the concentration

https://doi.org/10.1021/acsnano.5c10366
ACS Nano 2025, 19, 31224−31235

of MgS_x significantly decreased after adding Cu-HHTP. Specifically, S_8^{2-} and S_6^{2-} were completely adsorbed by Cu-HHTP-200, suggesting that the abundant mesopores play a key role in effectively capturing long-chain MgS_x. To elucidate the molecular-level binding mechanism, crystal orbital analysis and adsorption calculations were carried out to gain deeper insights into the binding behavior. Integrated crystal orbital Hamilton population (ICOHP) results in Figure 3b reveal that in nearly saturated coordinated Cu-HHTP, long-chain MgS_8 exhibits minimal bonding with Cu nodes (−0.09). In contrast, Cu-HHTP-O_d exhibits an ICOHP value of −1.54 for the Cu−S interaction, demonstrating substantially strengthened bonding between coordinatively unsaturated Cu centers and MgS_8. Furthermore, the selective adsorption capability was quantitatively assessed through calculated energy profiles of the consecutive conversion from S_8 to MgS (Figures 3c and S17). To further elucidate the interaction mechanism, adsorption energy calculations at distinct Cu coordination sites were conducted in Figure S18. Placement of the sulfur atom above the Cu center yields a significantly stronger adsorption energy (−1.34 eV) compared with that of the magnesium atom (−0.69 eV), indicating a preferential binding affinity between sulfur species and Cu sites. As a result, the undercoordinated Cu-HHTP-O_d exhibits markedly enhanced adsorption energy for MgS_x species. Therefore, enhancing the accessibility of active sites is essential to achieve the preconcentration of MgS_x at the interface.

Having established the strong polysulfide confinement and binding affinity, the catalytic conversion behavior of MgS_x species was further investigated using symmetric cell experiments in MgS_x electrolytes, which demonstrated reduced overpotential for Cu-HHTP-200, confirming its efficient catalytic activity (Figure 3d). To probe the role of the Cu-HHTP interlayer in regulating polysulfide conversion, *C*−*V* tests were performed. As shown in Figure 3e, S-Cu-HHTP shows a pronounced cathodic peak from 1.6 to 1.2 V. In contrast, S-Cu-HHTP-200 displays a broadened cathodic peak and enhanced current response (Figure 3f). After confirming that the Cu-HHTP-based interlayer solely functions as a catalytic medium without altering the sulfur conversion pathway (Figures S19−S23), a series of spectroscopic analyses were conducted to identify the multistep sulfur reduction products at the Cu-HHTP-200 interface.[31,36,37] The MS analysis in Figure 3g reveals that upon discharge to 1.2 V, a notable increase in polysulfide concentration was observed, suggesting an elevated active sulfur content anchored at the interlayer. A comprehensive compositional analysis of sulfur species was performed by Raman spectroscopy (Figure 3h). At 1.5 V, the spectrum was dominated by the peak at 401 cm^{-1}, attributed to S_6^{2-}.[1] Upon discharge to 1.2 V, intensified characteristic peaks at 198 and 256 cm^{-1} were observed, which can be assigned to the vibrational modes of S_4^{2-} species. The sequential reduction from S_6^{2-} to S_4^{2-} indicates promoted liquid−liquid conversion of long-chain MgS_x. This was further corroborated by XPS analysis (Figure 3i), which verified changes in the oxidation states of sulfur during discharge. According to Le Chatelier's principle, the accumulation of intermediate species shifts the reaction equilibrium toward further conversion of long-chain MgS_x, resulting in accelerated liquid-phase reaction kinetics and improved reaction reversibility.[7] Enhanced conversion from MgS_8 to MgS_4 not only limits the accumulation of long-chain intermediates but also enhances the redox current. Collectively, these effects underscore the role of the Cu-HHTP-200 interlayer in promoting interfacial MgS_x conversion and advancing the overall electrochemical performance of Mg−S batteries.

2.4. Kinetic Enhancement and Shuttle Suppression. To explore the role of mesoporous arrays in redox kinetics, a series of complementary electrochemical measurements were conducted. Electrochemical impedance spectroscopy (EIS) was first employed to evaluate the charge transfer resistance of different interlayer materials in Figure 4a. As the calcination temperature increased, the resistance gradually declined, with S-Cu-HHTP-200 exhibiting the lowest value among all samples. This reduction can be attributed to improved electrolyte infiltration and the formation of continuous electron pathways within the vertically aligned mesopores, effectively mitigating interfacial transport limitations.[38]

To gain deeper insight beyond interfacial resistance, we further decoupled the electronic and ionic transport behavior. Electron transfer kinetics were examined by analyzing Tafel slopes derived from cyclic voltammetry at varying scan rates (Figure 4b). Among all samples, S-Cu-HHTP-200 showed the lowest slope values for both Peak 1 and Peak 2, indicating the fastest electron transfer rate. Complementarily, the Mg^{2+} ion mobility was examined using the galvanostatic intermittent titration technique (GITT). As shown in Figure S24, the diffusion coefficient ($D_{Mg^{2+}}$) of S-Cu-HHTP-200@CNTs was nearly 1 order of magnitude higher than that of S-Cu-HHTP@CNTs during discharge, confirming that the mesoporous structure also accelerates ionic transport. In addition, the calcined Cu-HHTP materials exhibit predominant pseudocapacitive characteristics (Figures 4c and S25), which are beneficial for maintaining high-rate capability. These results collectively demonstrate that the mesoporous Cu-HHTP-200 architecture not only improves interfacial redox kinetics but also constructs a dual-function microenvironment for mass and charge transport.

Theoretical calculations were performed to investigate the mechanisms behind the enhanced catalytic kinetics of the mesoporous Cu-HHTP interlayer. Due to steric hindrance, Cu nodes in Cu-HHTP exhibit minimal chemical bond formation with MgS_8 or Mg_2S_8 (Figure S17), suggesting the insufficient long-chain polysulfide interaction.[39] For a comparison, in partial density of states (PDOS) analysis, the pronounced overlap of Cu-HHTP-O_d between Cu 3*d* and S 2*p* (p_y, p_z) orbitals indicates that the undercoordinated Cu−O configuration enables strong *d*−*p* orbital hybridization between Cu atoms and S atoms (Figure 4d). The enhanced orbital hybridization can be attributed to two key factors: (i) the reduced oxygen coordination number in Cu-HHTP-O_d weakens the tendency of Cu atoms to withdraw valence orbitals toward the nucleus, facilitating electron accommodation from sulfur species, and (ii) the accessible coordination sites exhibit reduced steric congestion.

In parallel with the enhanced electronic interactions, the mesoporous channels could function as a confined interfacial microenvironment that spatially immobilizes long-chain polysulfides (*e.g.*, MgS_8) and facilitates their stepwise conversion. The catalytic activity toward long-chain MgS_x conversion was evaluated by analyzing the Mg_2S_8 decomposition capability in Figure 4e. In the decomposed Mg_2S_8 configuration, the exposed Cu sites on Cu-HHTP-O_d effectively bond with sulfur, working synergistically with the O sites to achieve a pronounced anchoring effect on polysulfides. Furthermore, Cu-HHTP-O_d exhibits a lower

https://doi.org/10.1021/acsnano.5c10366
ACS Nano 2025, 19, 31224−31235

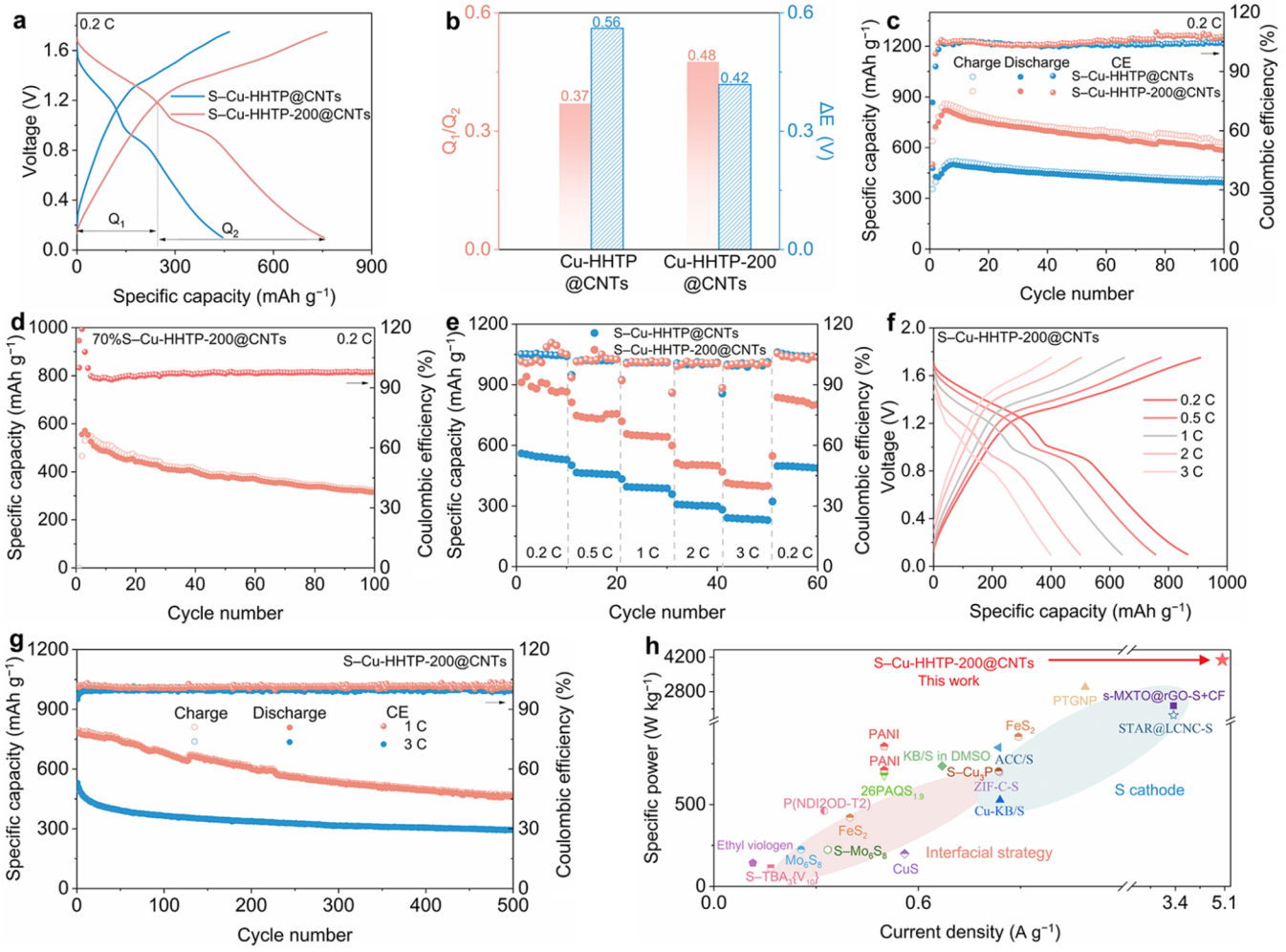

Figure 5. (a) Galvanostatic charge−discharge profiles at 0.2 C, (b) Q_1/Q_2 ratios and redox peak separation values obtained from galvanostatic tests. (c) Cycling stability at 0.2 C of S-Cu-HHTP@CNTs and S-Cu-HHTP-200@CNTs. (d) Cycling performance of 70%S-Cu-HHTP-200@CNTs at 0.2 C. (e) Rate capabilities of S-Cu-HHTP@CNTs and S-Cu-HHTP-200@CNTs. (f) Charge−discharge profiles at different rates of S-Cu-HHTP-200@CNTs. (g) Capacity retention of S-Cu-HHTP-200@CNTs at 1 C and 3 C. (h) Comparison of the specific power with different types of cathodes (refer to Table S4 for detailed data).

energy barrier for the Mg_2S_8 decomposition. Figure 4f depicts the variations in Mg−S bond lengths upon adsorption. Taking MgS_4 and Mg_2S_2 as examples, the formation of Cu−S bonds in Cu-HHTP-O_d with exposed Cu sites elongates the Mg−S bonds from 0.10 Å to 0.15 Å, compared to Cu-HHTP. The result rationalizes the observed lower polarization for conversion reactions. Therefore, the catalytic mechanism of the Cu-HHTP-O_d interlayer for sulfur reduction reactions is illustrated in Figure 4g. The well-developed mesoporous architecture enables spatial confinement and efficient enrichment of polysulfides. Within the mesopores, unsaturated Cu catalytic sites form robust *d*−*p* orbital hybridization with long-chain MgS_x species, which lowers the energy barrier for conversion and accelerates polysulfide consumption. This synergistic effect ensures effective utilization of the catalytic interface. It is noteworthy that the enhanced conversion from long-chain MgS_8 to MgS_4 not only contributes to the high-voltage plateau but also provides sufficient reactants for the conversion of short-chain species, which in turn, enhances the discharge capacity and energy density.

Building on the promoted MgS_x conversion at the catalytic interface, we further employed ICP analysis to evaluate the shuttle-suppression capability of the interlayer. Compared to S−PP, the sulfur content in the separator of S-Cu-HHTP exhibits a notable decrease (Figure 4h). Furthermore, the lower residual sulfur content of S-Cu-HHTP-200 exhibits enhanced sulfur confinement capability, highlighting the robust preconcentration effect within the mesoporous structure on polysulfides. Additionally, postcycling surface morphology of the electrodes with Cu-HHTP-200 interlayer is investigated by SEM (Figures S26 and S27). The S cathode exhibits a uniform particle distribution with sizes consistently below 5 μm throughout the charge−discharge processes, accompanied by minimal volume expansion. On the anode surface, the deposition of Mg is relatively uniform and dense, with a thickness of less than 1 μm. Such regulated interfacial behavior demonstrates that the electrocatalytic strategy effectively suppresses MgS_x shuttle effect and enhances the electrochemical reversibility at both electrodes. These findings highlight the advantages of interfacial coordination chemistry design in optimized anchoring effects and catalytic efficiency to effectively promote the conversion from MgS_8 to MgS_4, thereby boosting the kinetic performance and mitigating the shuttle effect.

2.5. Universality Evaluation of the Electrochemical Performance. To enhance conductivity and catalytic

https://doi.org/10.1021/acsnano.5c10366
ACS Nano 2025, 19, 31224−31235

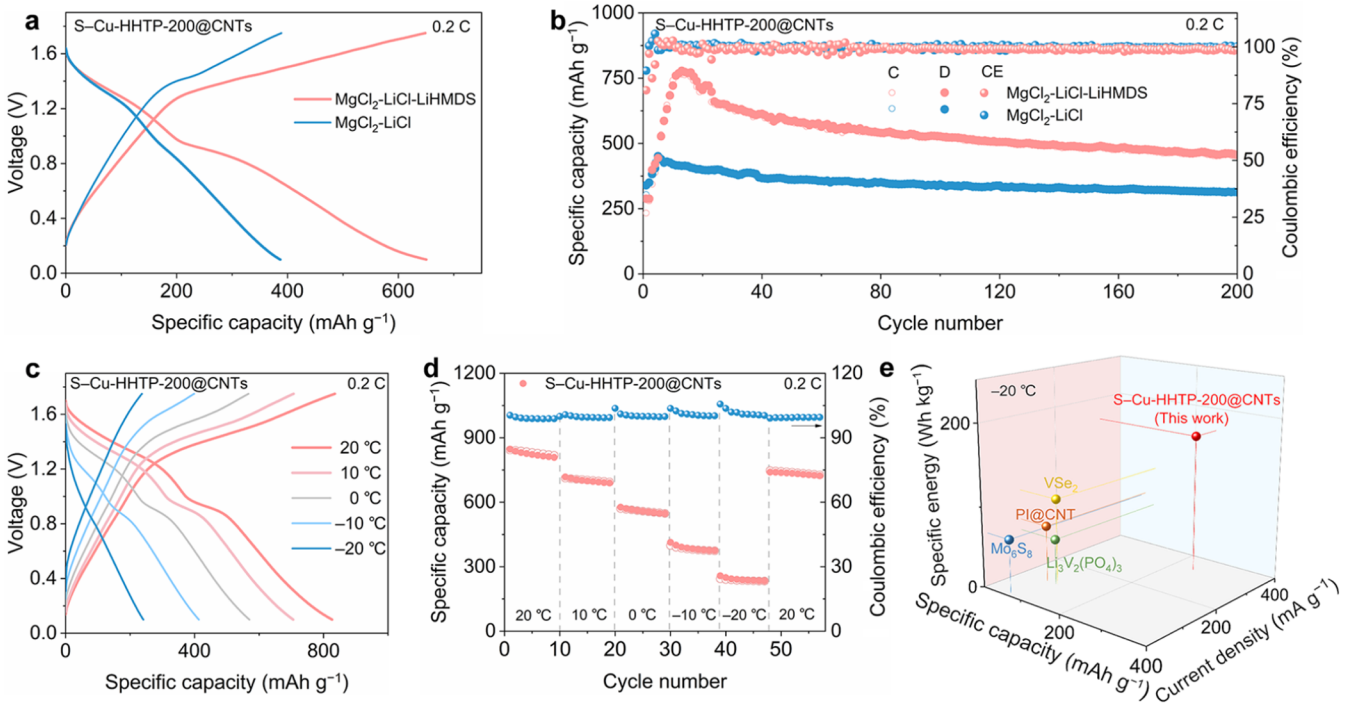

Figure 6. (a) Galvanostatic charge−discharge profiles, (b) cycling performance of S-Cu-HHTP-200@CNTs in different electrolytes at 0.2 C. (c) Galvanostatic charge−discharge profiles, (d) rate capabilities of S-Cu-HHTP-200@CNTs at different temperatures. (e) Comparative assessment of specific capacity, specific energy, and current density under −20 °C between S-Cu-HHTP-200@CNTs and previously reported cathodes in magnesium-ion batteries (see Table S5 for detailed data).

efficiency for broader applications, Cu-HHTP was loaded in situ on conductive substrates. Based on Cu-HHTP loading morphology and discharge capacities (Figures S28−S30), the carbon nanotube (CNT)-composited Cu-HHTP material emerged as the optimal catalyst for further studies, which could lead to a significant reduction in the charge transfer resistance from 3000 to 1000 ohms (Figure S30c). The galvanostatic charge−discharge profiles of Mg−S batteries with various catalytic interlayers at 0.2 C (Figure 5a) exhibited elevated voltage plateaus above 1.2 V. The polarization voltage (ΔE) was calculated from the average operating voltages of respective charge−discharge profiles. As expected, S-Cu-HHTP-200@CNTs demonstrated a significantly reduced polarization voltage ($\Delta E = 420$ mV) compared to S-Cu-HHTP@CNTs ($\Delta E = 560$ mV), as shown in Figure 5b. Of note, the capacity contribution from the high-voltage plateau (1.6−1.2 V) in the S-Cu-HHTP-200@CNT electrode is significantly enhanced, suggesting promoted conversion and more complete consumption of long-chain MgS_8 species. Consequently, the aforementioned analysis indicates that the mesoporous structure, abundant oxygen defects, and unsaturated Cu coordination sites in Cu-HHTP-200@CNTs facilitate rapid depletion of soluble MgS_x at elevated voltages, thereby enhancing the output voltage.

In long-cycle tests, S-Cu-HHTP-200@CNTs retain a high specific capacity of 585 mAh g^{-1} after 100 cycles at 0.2 C, indicating a significant suppression of the shuttle effect (Figure 5c). The observed increase in Coulombic efficiency and gradual decline in discharge capacity can be attributed to redox asymmetry during cycling. This asymmetry results from the incomplete reduction of MgS_x species during discharge and the partial reoxidation of residual polysulfides during charging.[40,41] To clarify whether the suppression of the shuttle effect stems from intrinsic features of Cu-HHTP-200@CNTs, we conducted a comparative study using a TiO_2 interlayer under identical electrochemical conditions. As shown in Figure S31, commercial rutile-phase TiO_2 exhibited a negligible effect on the conversion pathway, with electrochemical profiles resembling those of S−PP. The specific capacity of S−TiO_2 rapidly declined below 300 mAh g^{-1} within three cycles, confirming its limited capability in enhancing sulfur redox reversibility. Additional performance comparisons are presented in Table S3. In addition, postcycling SEM, XRD, and XPS characterizations (Figures S32−S34) confirm that the Cu-HHTP-200@CNT interlayer maintains its mesoporous architecture, crystallographic features, and stable Cu(I) oxidation state after extended cycling, supporting its electrochemical durability. These findings demonstrate that interfacial regulation through structural optimization and electronic modulation is more critical than conventional physical barriers in achieving the long-term stability of Mg−S batteries.

To achieve high-energy Mg−S batteries, we constructed cathodes with a high sulfur content of 70 wt %. The 70% S-Cu-HHTP-200@CNTs maintained a distinct high-voltage discharge plateau and a specific capacity exceeding 300 mAh g^{-1} (Figures 5d and S30d). While these results demonstrate promising performance, the degradation of capacity with increasing sulfur loading can be mainly attributed to the compromised interfacial contact, limited catalytic sites, and mechanical stress.[42,43] To further validate the practical feasibility, we increased the areal sulfur loading to 3 mg cm^{-2}, which resulted in stable cycling with an areal capacity of 0.9 mAh cm^{-2} over 200 cycles (Figure S35). Additionally, a prototype pouch cell with a total sulfur loading of 14 mg was assembled. This device exhibited an initial capacity of over 3 mAh and retained a clear high-voltage plateau at 1.6−1.2 V

https://doi.org/10.1021/acsnano.5c10366
ACS Nano 2025, 19, 31224−31235

throughout cycling, further demonstrating the compatibility of the interlayer (Figure S36).

Rate performance was evaluated to examine the kinetic stability under different current densities (Figure 5e). S-Cu-HHTP-200@CNTs demonstrate stable and consistent discharge plateaus across a wide range of current densities from 0.1 to 3 C (Figure 5f). Given the favorable rate performance, subsequent high-current cycling experiments were performed to verify its long-term applicability in high-power Mg−S batteries. As shown in Figure 5g, S-Cu-HHTP-200@CNTs retain a discharge capacity of 450 mAh g^{-1} after 500 cycles at 1 C. Even at a higher rate of 3 C, it still maintains 306 mAh g^{-1} after 500 cycles, corresponding to a high power density of 4090 W kg^{-1}. Control experiments confirmed that the catalyst contributes only 6% of the capacity at 1 C and 3 C (Figure S37), with sulfur redox reactions accounting for the dominant capacity. The performance comparison is summarized in Figure 5h and Table S4. These results support the interfacial catalytic approach as a route to durable, high-power Mg−S batteries.

The versatility of the catalytic interlayer was further evaluated in multiple electrolyte systems. In electrolytes composed of simple salts such as $MgCl_2$−LiCl and $MgCl_2$−LiCl−lithium bis(trimethylsilyl)amide (LiHMDS), S-Cu-HHTP-200@CNTs exhibit a well-defined high-voltage plateau associated with the conversion of long-chain MgS_x, indicating efficient redox kinetics (Figure 6a). Notably, in the $MgCl_2$−LiCl−LiHMDS electrolyte, the cell maintains a high discharge capacity of 454 mAh g^{-1} after 200 cycles at 0.2 C. It also exhibits a stable Coulombic efficiency close to 100% (Figure 6b), confirming the robustness of the interlayer under extended cycling. Furthermore, in lithium−sulfur (Li−S) batteries, S-Cu-HHTP-200@CNTs also demonstrated prolonged high-voltage plateaus and enhanced discharge specific capacity, enabling higher specific energy compared to S−PP (Figure S38). These findings collectively verify the universal effectiveness of the catalytic interlayer in promoting conversion kinetics and mitigating the shuttle effect across various electrolyte systems.

To further evaluate the catalytic role of the interlayer in promoting the conversion kinetics, S-Cu-HHTP-200@CNTs were tested under LT conditions, which could address a critical gap in Mg−S batteries for cold-region electric equipment applications.[44] Rate performance at different temperatures was conducted, as shown in Figure 6c,d. The S-Cu-HHTP-200@CNTs demonstrate LT tolerance, maintaining a high discharge plateau from 1.6 to 1.2 V and delivering a specific capacity exceeding 200 mAh g^{-1} even at −20 °C. At this temperature, both the specific capacity and the specific energy of S-Cu-HHTP-200@CNTs exceed those reported for most magnesium-ion batteries (Figure 6e and Table S5). Hence, the Cu-HHTP-200@CNT catalytic interlayer effectively suppresses the shuttle effect due to its strong anchoring interactions. Additionally, it facilitates the reduction of long-chain MgS_x, which in turn, enhances both the output voltage and the kinetic properties. These advances enable Mg−S batteries to operate reliably over a broad temperature window, underscoring their promise for practical deployment.

3. CONCLUSIONS

In summary, Cu-HHTP-200@CNTs with vertical mesoporous arrays were developed as a catalytic interlayer for Mg−S batteries. The sluggish reduction kinetics of long-chain MgS_8 have been identified as the primary cause of capacity deterioration in the S cathode. The Cu-HHTP-200 electrocatalyst, engineered with a hierarchical porous structure, abundant oxygen defects, and exposed Cu sites, enables efficient local electronic structure modulation at Cu sites. This structural advantage facilitates the conversion of long-chain MgS_x at higher voltages and alleviates the shuttle effect. Consequently, Mg−S batteries incorporating the Cu-HHTP-200@CNT interlayer demonstrate a power density of 4090 W kg^{-1} after 500 cycles and a high specific capacity of 236 mAh g^{-1} even at −20 °C. The results provide insights regarding the effects of the coordination environment within π−d conjugated MOFs on stepwise sulfur conversion and present an interfacial engineering strategy for high-performance sulfur-based batteries.

4. EXPERIMENTAL SECTION

4.1. Synthesis of Cu-HHTP and Its Derivatives. In a typical synthesis procedure, 0.233 g of HHTP ligand was ultrasonically dissolved in a mixture of 3 mL of *N*,*N*-dimethylformamide (DMF) and 24 mL of H_2O, then slowly added to a solution of $CuSO_4{\cdot}5H_2O$ in 9 mL of H_2O. The mixture was stirred for 15 min before being transferred to an autoclave and heated at 85 °C for 12 h. The obtained blue-black powder was washed twice with H_2O, ethanol, and acetone and then dried in a vacuum oven at 60 °C overnight. The synthesis of Zn-HHTP followed the same procedure as Cu-HHTP, with the substitution of copper sulfate by zinc acetate. The obtained Cu-HHTP powder was calcined at a heating rate of 2 °C min^{-1} to 150, 200, 250, and 300 °C for 2 h under an argon atmosphere, yielding Cu-HHTP-150, Cu-HHTP-200, Cu-HHTP-250, and Cu-HHTP-300, respectively.

4.2. Synthesis of the Composites of Cu-HHTP and Conductive Substrates. Composites of Cu-HHTP with graphene (G), graphene oxide (GO), and CNTs were synthesized by applying the same treatment steps used for Cu-HHTP, with the additional incorporation of 30% G/GO/CNTs in the precursor solution prior to hydrothermal treatment. Specifically, 0.5 g of $CuSO_4{\cdot}5H_2O$ was dissolved in 4.5 mL of H_2O, and 37.5 mg of CNTs was dispersed in a mixture of 1.5 mL of DMF and 12 mL of H_2O. Subsequently, 0.1165 g of HHTP was introduced into the mixture under ultrasonic conditions. The reaction mixture was then hydrothermally treated in an autoclave at 85 °C for 12 h, followed by washing and vacuum-drying.

4.3. Fabrication of Cu-HHTP-Based Interlayers. The Cu-HHTP/Cu-HHTP-200@CNTs, Ketjen Black, and poly(vinylidene fluoride) binder (in a weight ratio of 7:2:1) were mixed with *N*-methyl-2-pyrrolidone in a mortar. The homogeneous slurry was then cast onto a PP/PE/PP (abbreviated as PP) interlayer and dried at 80 °C overnight. The dried samples were cut into interlayers with a diameter of 19 mm. The mass loading was approximately 0.3 mg cm^{-2}.

ASSOCIATED CONTENT

Supporting Information

The Supporting Information is available free of charge at https://pubs.acs.org/doi/10.1021/acsnano.5c10366.

Materials; electrochemical measurement configurations; characterization and computational methods; electrolyte characterizations; SEM/TEM/XRD/XPS/TG of the S cathode; SEM/TEM/XPS/EXAFS of Cu-HHTP and its derivatives; DFT models of polysulfides with Cu-HHTP and Cu-HHTP-O_d substrates; C−V curves and EIS spectra of the S cathode with various interlayers; ex situ XPS and XRD of the Cu-HHTP interlayer and its derivative; kinetic evaluation of the S cathode with various interlayers; SEM images of electrodes; SEM/

https://doi.org/10.1021/acsnano.5c10366
ACS Nano 2025, 19, 31224−31235

XRD/BET of Cu-HHTP loaded on different conductive substrates; galvanostatic charge−discharge profiles of S−CNTs, S-Cu-HHTP-O_d@CNTs, and S−TiO_2; ex situ SEM/XRD/XPS of the cycled interlayer; and electrochemical performance of the pouch cell, Cu-HHTP-200@CNT-SS electrodes, S−PP, and S-Cu-HHTP-200@CNTs in Li−S batteries (PDF)

AUTHOR INFORMATION

Corresponding Author

Xuebin Yu − *Department of Materials Science, Fudan University, Shanghai 200433, China;* orcid.org/0000-0002-4035-0991; Email: yuxuebin@fudan.edu.cn

Authors

Xian Zhou − *Department of Materials Science, Fudan University, Shanghai 200433, China*

Tian Xu − *Department of Materials Science, Fudan University, Shanghai 200433, China*

Miao Guo − *Department of Materials Science, Fudan University, Shanghai 200433, China*

Hongyu Zhang − *Department of Materials Science, Fudan University, Shanghai 200433, China*

Chaoqun Li − *Department of Materials Science, Fudan University, Shanghai 200433, China*

Wenbin Wang − *Department of Materials Science, Fudan University, Shanghai 200433, China*

Ming Sun − *Department of Materials Science, Fudan University, Shanghai 200433, China*

Guanglin Xia − *Department of Materials Science, Fudan University, Shanghai 200433, China;* orcid.org/0000-0002-3493-4309

Complete contact information is available at: https://pubs.acs.org/10.1021/acsnano.5c10366

Notes

The authors declare no competing financial interest.

ACKNOWLEDGMENTS

This work was partially supported by the National Natural Science Foundation of China (51971065, 52301265).

REFERENCES

(1) Luo, T.; Wang, Y.; Elander, B.; Goldstein, M.; Mu, Y.; Wilkes, J.; Fahrenbruch, M.; Lee, J.; Li, T.; Bao, J. L.; Mohanty, U.; Wang, D. Polysulfides in Magnesium-Sulfur Batteries. *Adv. Mater.* **2024**, *36*, No. 2306239.

(2) Liang, Y.; Dong, H.; Aurbach, D.; Yao, Y. Current Status and Future Directions of Multivalent Metal-Ion Batteries. *Nat. Energy* **2020**, *5*, 646−656.

(3) Blázquez, J. A.; Maça, R. R.; Leonet, O.; Azaceta, E.; Mukherjee, A.; Zhao-Karger, Z.; Li, Z.; Kovalevsky, A.; Fernández-Barquín, A.; Mainar, A. R.; Jankowski, P.; Rademacher, L.; Dey, S.; Dutton, S. E.; Grey, C. P.; Drews, J.; Häcker, J.; Danner, T.; Latz, A.; Sotta, D.; Palacin, M. R.; Martin, J.-F.; Lastra, J. M. G.; Fichtner, M.; Kundu, S.; Kraytsberg, A.; Ein-Eli, Y.; Noked, M.; Aurbach, D. A Practical Perspective on the Potential of Rechargeable Mg Batteries. *Energy Environ. Sci.* **2023**, *16*, 1964−1981.

(4) He, P.; Schaefer, J. L. The Key Role of Magnesium Polysulfides in the Development of Mg−S Batteries. *ACS Energy Lett.* **2022**, *7*, 4352−4361.

(5) Zou, Q.; Sun, Y.; Liang, Z.; Wang, W.; Lu, Y. C. Achieving Efficient Magnesium−Sulfur Battery Chemistry Via Polysulfide Mediation. *Adv. Energy Mater.* **2021**, *11*, No. 2101552.

(6) Liu, R.; Wei, Z.; Peng, L.; Zhang, L.; Zohar, A.; Schoeppner, R.; Wang, P.; Wan, C.; Zhu, D.; Liu, H.; Wang, Z.; Tolbert, S. H.; Dunn, B.; Huang, Y.; Sautet, P.; Duan, X. Establishing Reaction Networks in the 16-Electron Sulfur Reduction Reaction. *Nature* **2024**, *626*, 98−104.

(7) Li, H.; Meng, R.; Ye, C.; Tadich, A.; Hua, W.; Gu, Q.; Johannessen, B.; Chen, X.; Davey, K.; Qiao, S.-Z. Developing High-Power Li||S Batteries Via Transition Metal/Carbon Nanocomposite Electrocatalyst Engineering. *Nat. Nanotechnol.* **2024**, *19*, 792−799.

(8) Yang, Y.; Fu, W.; Zhang, D.; Ren, W.; Zhang, S.; Yan, Y.; Zhang, Y.; Lee, S.-J.; Lee, J.-S.; Ma, Z.-F.; Yang, J.; Wang, J.; NuLi, Y. Toward High-Performance Mg−S Batteries Via a Copper Phosphide Modified Separator. *ACS Nano* **2023**, *17*, 1255−1267.

(9) Guan, Q.; Wang, J.; Zhuang, Q.; Zhang, J.; Li, L.; Jia, L.; Zhang, Y.; Hu, H.; Hu, H.; Cheng, S.; Zhang, H.; Li, H.; Liu, M.; Wang, S.; Lin, H. Self-Tandem Catalysis of Fast Mg^{2+} Desolvation and Sulfur Conversions for Ultrahigh-Performance Mg−S Batteries Via Serially-Assembled Atomic Reactors. *Energy Environ. Sci.* **2024**, *17*, 3765−3775.

(10) Wang, X.; Zhang, X.; Zhao, Y.; Luo, D.; Shui, L.; Li, Y.; Ma, G.; Zhu, Y.; Zhang, Y.; Zhou, G.; Yu, A.; Chen, Z. Accelerated Multi-Step Sulfur Redox Reactions in Lithium-Sulfur Batteries Enabled by Dual Defects in Metal-Organic Framework-Based Catalysts. *Angew. Chem., Int. Ed.* **2023**, *62*, No. e202306901.

(11) Zhou, X.; Tian, J.; Hu, J.; Li, C. High Rate Magnesium-Sulfur Battery with Improved Cyclability Based on Metal-Organic Framework Derivative Carbon Host. *Adv. Mater.* **2018**, *30*, No. 1704166.

(12) Guo, M.; Yuan, C.; Xu, T.; Zhong, S.; Wang, W.; Zou, T.; Zhang, T.; Yu, X. In Situ Built Nanoconfined TiO_2 Particles in Robust-Flexible MXene@rGO Conductive Framework Enabling High-Performance Hybrid Magnesium−Sulfur Batteries. *Adv. Energy Mater.* **2023**, *13*, No. 2300417.

(13) Guo, Y.; Niu, Q.; Pei, F.; Wang, Q.; Zhang, Y.; Du, L.; Zhang, Y.; Zhang, Y.; Zhang, Y.; Fan, L.; Zhang, Q.; Yuan, L.; Huang, Y. Interface Engineering toward Stable Lithium−Sulfur Batteries. *Energy Environ. Sci.* **2024**, *17*, 1330−1367.

(14) Su, Y.-S.; Manthiram, A. Lithium−Sulphur Batteries with a Microporous Carbon Paper as a Bifunctional Interlayer. *Nat. Commun.* **2012**, *3*, No. 1166.

(15) Yang, D.; Liang, Z.; Tang, P.; Zhang, C.; Tang, M.; Li, Q.; Biendicho, J. J.; Li, J.; Heggen, M.; Dunin-Borkowski, R. E.; Xu, M.; Llorca, J.; Arbiol, J.; Morante, J. R.; Chou, S. L.; Cabot, A. A High Conductivity 1D π−d Conjugated Metal−Organic Framework with Efficient Polysulfide Trapping-Diffusion-Catalysis in Lithium−Sulfur Batteries. *Adv. Mater.* **2022**, *34*, No. 2108835.

(16) Zhang, Q.; Jiang, S.; Lv, T.; Peng, Y.; Pang, H. Application of Conductive MOF in Zinc-Based Batteries. *Adv. Mater.* **2023**, *35*, No. 2305532.

(17) Xie, L. S.; Skorupskii, G.; Dincă, M. Electrically Conductive Metal−Organic Frameworks. *Chem. Rev.* **2020**, *120*, 8536−8580.

(18) Fan, K.; Zhang, C.; Chen, Y.; Wu, Y.; Wang, C. The Chemical States of Conjugated Coordination Polymers. *Chem.* **2021**, *7*, 1224−1243.

(19) Tao, S.; Wang, J.; Zhang, J. Conductive Metal−Organic Frameworks and Their Electrocatalysis Applications. *ACS Nano* **2025**, *19*, 9484−9512.

(20) Yang, D.; Wang, J.; Lou, C.; Li, M.; Zhang, C.; Ramon, A.; Li, C.; Tang, M.; Henkelman, G.; Xu, M.; Li, J.; Llorca, J.; Arbiol, J.; Mitlin, D.; Zhou, G.; Cabot, A. Single-Atom Catalysts with Unsaturated Co−N_2 Active Sites Based on a C_2N 2D-Organic Framework for Efficient Sulfur Redox Reaction. *ACS Energy Lett.* **2024**, *9*, 2083−2091.

(21) Xiao, Y.; Guo, S.; Ouyang, Y.; Li, D.; Li, X.; He, W.; Deng, H.; Gong, W.; Tan, C.; Zeng, Q.; Zhang, Q.; Huang, S. Constructing Heterogeneous Structure in Metal−Organic Framework-Derived Hierarchical Sulfur Hosts for Capturing Polysulfides and Promoting Conversion Kinetics. *ACS Nano* **2021**, *15*, 18363−18373.

(22) Zhang, Y.; Wang, W.; Jia, Z.; Ding, J.; Hua, L.; Sun, M.; Li, Y.; Wang, G.; Li, C. Dual-Stage Polyporate Framework with Redox

Mediator for High Loading Lithium Sulfur Batteries. *Energy Storage Mater.* **2024**, *67*, No. 103320.
(23) Muthuraj, D.; Pandey, M.; Krishna, M.; Ghosh, A.; Sen, R.; Johari, P.; Mitra, S. Magnesium Polysulfide Catholyte (MgS_x): Synthesis, Electrochemical and Computational Study for Magnesium-Sulfur Battery Application. *J. Power Sources* **2021**, *486*, No. 229326.
(24) Gao, T.; Ji, X.; Hou, S.; Fan, X.; Li, X.; Yang, C.; Han, F.; Wang, F.; Jiang, J.; Xu, K.; Wang, C. Thermodynamics and Kinetics of Sulfur Cathode During Discharge in $MgTFSI_2$−DME Electrolyte. *Adv. Mater.* **2018**, *30*, No. 1704313.
(25) Robba, A.; Vizintin, A.; Bitenc, J.; Mali, G.; Arčon, I.; Kavčič, M.; Žitnik, M.; Bučar, K.; Aquilanti, G.; Martineau-Corcos, C.; Randon-Vitanova, A.; Dominko, R. Mechanistic Study of Magnesium−Sulfur Batteries. *Chem. Mater.* **2017**, *29*, 9555−9564.
(26) Zheng, D.; Wang, G.; Liu, D.; Si, J.; Ding, T.; Qu, D.; Yang, X.; Qu, D. The Progress of Li−S Batteries—Understanding of the Sulfur Redox Mechanism: Dissolved Polysulfide Ions in the Electrolytes. *Adv. Mater. Technol.* **2018**, *3*, No. 1700233.
(27) Ren, X.; Wang, Q.; Pu, Y.; Sun, Q.; Sun, W.; Lu, L. Synergizing Spatial Confinement and Dual-Metal Catalysis to Boost Sulfur Kinetics in Lithium−Sulfur Batteries. *Adv. Mater.* **2023**, *35*, No. 2304120.
(28) Lv, Q.; Sun, Y.; Li, B.; Li, C.; Zhang, Q.; Wang, L. Metal−Organic Frameworks with Axial Cobalt−Oxygen Coordination Modulate Polysulfide Redox for Lithium−Sulfur Batteries. *Adv. Energy Mater.* **2024**, *14*, No. 2403223.
(29) Lu, H.; Zeng, Q.; Xu, L.; Xiao, Y.; Xie, L.; Yang, J.; Rong, J.; Weng, J.; Zheng, C.; Zhang, Q.; Huang, S. Multimodal Engineering of Catalytic Interfaces Confers Multi-Site Metal-Organic Framework for Internal Preconcentration and Accelerating Redox Kinetics in Lithium-Sulfur Batteries. *Angew. Chem., Int. Ed.* **2024**, *63*, No. e202318859.
(30) Sun, Y.; Ji, H.; Sun, Y.; Zhang, G.; Zhou, H.; Cao, S.; Liu, S.; Zhang, L.; Li, W.; Zhu, X.; Pang, H. Synergistic Effect of Oxygen Vacancy and High Porosity of Nano MIL-125(Ti) for Enhanced Photocatalytic Nitrogen Fixation. *Angew. Chem., Int. Ed.* **2023**, *63*, No. e202316973.
(31) Li, Z.; Li, Y.; Zhan, Y.; Lin, X.; Yao, Y.; Zhao, T.; Sun, F.; Xu, H.; Ma, Z.; Zhang, W.; Xue, Y.; Li, X.; Vlad, A.; Zou, J. On the Origin of Capacity Increase in Rechargeable Magnesium Batteries with Manganese Oxide Cathodes and Copper Metal Current Collectors. *Angew. Chem., Int. Ed.* **2025**, *64*, No. e202416960.
(32) Qi, S. C.; Qian, X. Y.; He, Q. X.; Miao, K. J.; Jiang, Y.; Tan, P.; Liu, X. Q.; Sun, L. B. Generation of Hierarchical Porosity in Metal−Organic Frameworks by the Modulation of Cation Valence. *Angew. Chem., Int. Ed.* **2019**, *58*, 10104−10109.
(33) Yang, M.; Zeng, X.; Xie, M.; Wang, Y.; Xiao, J.-M.; Chen, R.-H.; Yi, Z.-J.; Huang, Y.-F.; Bin, D.-S.; Li, D. Conductive Metal−Organic Framework with Superior Redox Activity as a Stable High-Capacity Anode for High-Temperature K-Ion Batteries. *J. Am. Chem. Soc.* **2024**, *146*, 6753−6762.
(34) Yin, J. C.; Lian, X.; Li, Z. G.; Cheng, M.; Liu, M.; Xu, J.; Li, W.; Xu, Y.; Li, N.; Bu, X. H. Triazacoronene-Based 2D Conductive Metal−Organic Framework for High-Capacity Lithium Storage. *Adv. Funct. Mater.* **2024**, *34*, No. 2403656.
(35) Wang, J.; Mueller, D. N.; Crumlin, E. J. Recommended Strategies for Quantifying Oxygen Vacancies with X-Ray Photoelectron Spectroscopy. *J. Eur. Ceram. Soc.* **2024**, *44*, No. 116709.
(36) He, P.; Ford, H. O.; Merrill, L. C.; Schaefer, J. L. Investigation of the Effects of Copper Nanoparticles on Magnesium−Sulfur Battery Performance: How Practical Is Metallic Copper Addition? *ACS Appl. Energy Mater.* **2019**, *2*, 6800−6807.
(37) Zhang, R.; Cui, C.; Xiao, R.; Li, R.; Mu, T.; Huo, H.; Ma, Y.; Yin, G.; Zuo, P. Interface Regulation of Mg Anode and Redox Couple Conversion in Cathode by Copper for High-Performance Mg−S Battery. *Chem. Eng. J.* **2023**, *451*, No. 138663.
(38) Chen, J.; Li, G.; Bu, F.; Tian, J.; Liu, L.; Wang, Y.; Zhang, J.; Li, X.; Li, X.; Yang, Z.; Chao, D.; Zhao, D. Tandem Assembly and Etching Chemistry Towards Mesoporous Conductive Metal-Organic Frameworks for Sodium Storage over 50,000 Cycles. *Angew. Chem., Int. Ed.* **2025**, *64*, No. e202500287.
(39) Wang, J.; Zhang, X.; Wang, X.; Liu, J.; Li, S.; Nie, Y.; Zong, K.; Zhang, X.; Meng, H.; Jin, M.; Yang, L.; Wang, X.; Chen, Z. Activation of MOF Catalysts with Low Steric Hindrance Via Undercoordination Chemistry for Efficient Polysulfide Conversion in Lithium−Sulfur Battery. *Adv. Energy Mater.* **2024**, *14*, No. 2402072.
(40) Gao, T.; Hou, S.; Wang, F.; Ma, Z.; Li, X.; Xu, K.; Wang, C. Reversible S^0/MgS_x Redox Chemistry in a $MgTFSI_2/MgCl_2$/DME Electrolyte for Rechargeable Mg/S Batteries. *Angew. Chem., Int. Ed.* **2017**, *56*, 13526−13530.
(41) Sheha, E.; Farrag, M.; Fan, S.; Kamar, E.; Sa, N. A Simple Cl−Free Electrolyte Based on Magnesium Nitrate for Magnesium−Sulfur Battery Applications. *ACS Appl. Energy Mater.* **2022**, *5*, 2260−2269.
(42) Zhao-Karger, Z.; Zhao, X.; Wang, D.; Diemant, T.; Behm, R. J.; Fichtner, M. Performance Improvement of Magnesium Sulfur Batteries with Modified Non-Nucleophilic Electrolytes. *Adv. Energy Mater.* **2014**, *5*, No. 1401155.
(43) Bieker, G.; KüPers, V.; Kolek, M.; Winter, M. Intrinsic Differences and Realistic Perspectives of Lithium-Sulfur and Magnesium-Sulfur Batteries. *Commun. Mater.* **2021**, *2*, No. 37.
(44) Guo, L.; Chen, A.; Wang, A.; Hu, Z.; Zhang, H.; Luo, J. Rechargeable Mg−Br_2 Battery with Ultrafast Bromine Chemistry. *J. Am. Chem. Soc.* **2024**, *146*, 26855−26862.

https://doi.org/10.1021/acsnano.5c10366
ACS Nano 2025, 19, 31224−31235